



Large eddy simulation of fluid injection under transcritical and supercritical conditions

Wu Wei, Maozhao Xie, and Ming Jia

School of Energy and Power Engineering, Dalian University of Technology, Dalian City, P. R. China

ABSTRACT

When a cryogenic fluid initially at a subcritical temperature is injected into a supercritical environment, it will experience a process across a pseudo-boiling point, at which the specific heat reaches its maximum value under the corresponding pressure. Large eddy simulation (LES) is conducted to explore the effects of pseudo-vaporization phenomenon around the pseudo-critical temperature on fluid jet evolution. To highlight the pseudo-vaporization effect, a cryogenic nitrogen jet with different injection temperatures, which correspond to transcritical and supercritical conditions, respectively, is injected into a chamber with same supercritical conditions. All of the thermophysical and transport properties are determined directly from fundamental theories combined with a real fluid equation of state. It is found that when the fluid transits through the pseudo-boiling point, the constant-pressure specific heat reaches a local maximum, while the thermal conductivity and viscosity become minimum. The condition-averaged constant-pressure specific heat suggests that the pseudo-boiling point has the effect of increasing the density gradients. Vorticity and Q -criterion analysis reveals that high-temperature injection facilitates the mixing of jet fluid with ambient gas. Also, the high-temperature injection of supercritical fluid can earlier transit into the full developed region.

ARTICLE HISTORY

Received 25 February 2016

Accepted 27 May 2016

1. Introduction

Presently, many combustion devices operate at a high pressure and in a wide range of temperatures, in which fluid thermodynamic properties undergo the phenomenon of transition from a subcritical to supercritical state. If you take the rocket engines for example, the pressure and temperature in the combustion chambers is considerably high and well above the critical point of the injected propellants. By increasing the chamber pressure, a higher specific impulse is obtained and finally results in an increase of the efficiency of the engine. In addition, supercritical combustion conditions have the effects of reducing emissions of pollution gases. In case of modern internal combustion engine, the combustion chamber pressure and temperature are usually above the critical point of the fuel, while the fuel injection temperature may be subcritical or supercritical, that can be called transcritical injection [1] and supercritical injection, respectively, because in the former case the fuel experiences a transition from the subcritical state to the supercritical one during the injection, while in the latter case the fuel is always in supercritical state.

It has been widely accepted that when the thermodynamic state of a fluid exceeds the critical point, the distinctions between gases and liquids vanish, and hence only a single fluid phase is defined, which is referred to as supercritical fluid. The traditional point of view is that the thermophysical properties of supercritical fluids are between those of gas and liquid with liquid-like density and gas-like transport

Nomenclature

E_p^H	slope of the linear regression	T_c	critical pressure
EOS	equation of state	T_{inj}	inject temperature
e_t	total energy	T_∞	environment temperature
H	energy flux	t	time
H_i^{SGS}	sub-grid scale energy fluxes	θ^H	HWHM spreading angle
LES	large eddy simulation	ρ_{inj}	inject density
L_p	half-width	ρ_c	critical density
P	pressure	ρ_∞	environment density
P_c	critical pressure	$\nabla \rho$	density gradient
R	universal gas constant	Δ	filter width
S_{ij}^{SGS}	sub-grid scale strain-rate tensor	ω	acentric factor
SRK	Soave–Redlich–Kwong	τ_{ij}	sheer stress
T	temperature	σ_{ij}	viscous work

properties. However, recent investigations [2, 3] have demonstrated that supercritical fluid states are not homogeneously distributed, but can be divided into two different regions with gas-like and liquid-like behaviors, much like the situations at subcritical conditions. These regions are separated by an extension of the coexisting line, the so-called Widom line.

Around the pseudo-boiling point, or strictly speaking, around the Widom line, transport and thermodynamics properties of a fluid are very sensible to the temperature. Thus, slight changes in temperature may result in large variation of thermodynamics and transport properties, which in turn influence the jet evolution. Moreover, the solubility of gases into the liquid phase and multi-component phase equilibrium should be considered under such high-pressure conditions. In this situation, special methods should be applied to evaluate thermodynamics and transport properties. Therefore, understanding the fluid injection and mixing features under trans-/supercritical conditions is significantly important for designing high-performance combustion devices.

Extensive experimental studies [4–10] were conducted by Mayer, Oswald, Cheroudi, and coworkers with single or multi-component fluids injected into the chamber under supercritical conditions. These experiments indicate that as the pressure increases to supercritical state, the surface tension is intensively decreased and the boundary between liquid jet and ambient gas is obscured. Besides, the classical breakup and atomization process in subcritical regime cannot be seen in supercritical regime, so drops and liquid ligaments are no longer detected but finger-like structures emerging from the jet core. Compared to experimental study, numerical simulation is considered an effective method to explore mixing characteristics and jet evolution. Miller et al. [11, 12] and Okong'O and Bellan [13] conducted comprehensive researches on the trans-/supercritical mixing layer using a direct numerical simulation (DNS) approach. They show that the Soret and Dufour impacts have certain effects on jet evolution and should not be neglected under supercritical conditions. Oefelin [14] investigated transcritical sprays using large eddy simulation (LES), and the equations were closed by the universal Smagorinsky subgrid model that is suitable for low-pressure conditions. Zong et al. [15] and Zong and Yang [16] made great effort to explore a preconditioning scheme incorporating a unified treatment of general fluid thermodynamics and simulated spray injection of cryogenic nitrogen into supercritical state by means of LES. They suggest that the density gradient has the effects of stabilizing jet evolution. Kim [17] proposed a specific turbulent model for supercritical flow, while Park [18] conducted a simulation based on several turbulent models and compared with LES results. They indicated that turbulent models have limited influence on the jet evolution, while the suitable adoption of real fluid equation of state plays an important role on the numerical simulation. More extensive numerical investigations are available in the literature [19–24].

As mentioned earlier, injections of fluid with temperature below or above the critical point into a supercritical environment correspond to the transcritical and supercritical injection respectively. Different initial temperatures may have great influence on the evolution of injection flow, here the

pseudo-boiling phenomenon is of particular relevance, which has not been deeply understood. Yin and Lu [25] investigated the effect of injection temperature on jet evolution under supercritical conditions by means of a LES method. However, they used a two-dimensional model, which inherently neglected the vortex stretching mechanism. Such vortex stretching mechanism facilitates energy transfer from large to small scales through the continuous generation of small-scale vortices. Since the small scales are responsible for the dissipation of energy, the two-dimensional model will lead to lower-energy dissipation and turbulence production rates during jet evolution.

Comparing to conventional RANS method, LES methods predict relative accurate values and have the capacity of capturing the detailed characteristics of the flow field, so numerous studies [26–29] have been conducted by LES in the past decades. In the present work, a comparative study on the transcritical and supercritical injections of a cryogenic fluid is carried out using LES. All the thermodynamic and transport properties are derived directly from a real fluid equation of state. The purpose of this work is to reveal the mixing mechanisms and flow evolution behaviors under different initial temperatures with emphasis on the intensive variations of thermophysical and transport properties and the effect of the pseudo-boiling phenomenon.

2. Governing equations and thermodynamic properties

To derive the LES equations, a filtering operator is applied to the set of N-S equations. The filtered conservative variable vector is $\bar{\varphi} = (\bar{\rho}, \bar{\rho}u_i, \bar{\rho}e_t)$, which can also be written in terms of Favre-averaged variables: $\bar{\varphi} = (\bar{\rho}, \bar{\rho}\tilde{u}_i, \bar{\rho}\tilde{e}_t)$, and the subscript i denotes the velocity component in i direction. Thus, the set of LES equations for single-species fluid injection can be expressed as,

$$\frac{\partial \bar{\rho}}{\partial t} + \frac{\partial (\bar{\rho}\tilde{u}_i)}{\partial x_i} = 0 \quad (1)$$

$$\frac{\partial (\bar{\rho}\tilde{u}_i)}{\partial t} + \frac{\partial (\bar{\rho}\tilde{u}_i\tilde{u}_j + \bar{p}\delta_{ij})}{\partial x_j} = \frac{\partial (\bar{\tau}_{ij} - \tau_{ij}^{\text{SGS}})}{\partial x_j} \quad (2)$$

$$\frac{\partial \bar{\rho}\tilde{e}_t}{\partial t} + \frac{\partial [(\bar{\rho}\tilde{e}_t + \bar{p})\tilde{u}_i]}{\partial x_i} = \frac{\partial [\tilde{u}_j\bar{q}_i - H_i^{\text{SGS}} + \sigma_i^{\text{SGS}}]}{\partial x_i} \quad (3)$$

where ρ , u_i , p , τ_{ij} , e_t represent the density, velocity components, pressure, viscous stress tensor, and total energy, respectively. The overbars and tildes over the variables denote the resolved-scale and Favre-averaged resolved-scale, respectively. The unclosed subgrid-scale (SGS) terms arising from spatial filtering in Eqs. (1)–(3), including the stresses τ_{ij}^{SGS} , energy fluxes H_i^{SGS} , and viscous work σ_{ij}^{SGS} are defined as

$$\tau_{ij}^{\text{SGS}} = (\overline{\rho u_i u_j} - \bar{\rho}\tilde{u}_i\tilde{u}_j) \quad (4)$$

$$H_{ij}^{\text{SGS}} = (\overline{\rho e_t u_i} - \bar{\rho}\tilde{e}_t\tilde{u}_i) + (\overline{\rho u_i} - \bar{\rho}\tilde{u}_i) \quad (5)$$

$$\sigma_{ij}^{\text{SGS}} = (\overline{u_j \tau_{ij}} - \tilde{u}_j \bar{\tau}_{ij}) \quad (6)$$

These SGS terms are not closed and need to be modeled based on the resolved scales quantities. There are various subgrid models available for compressible flow, including the classical Smagorinsky model [30] and dynamic Smagorinsky model [31]. For the Smagorinsky model, the stress term is defined as

$$\tau_{ij}^{\text{SGS}} = -2\nu_t \bar{\rho} \left(\tilde{S}_{ij} - \frac{\tilde{S}_{kk}\delta_{ij}}{3} \right) + \frac{2}{3} \bar{\rho} k^{\text{SGS}} \delta_{ij} \quad (7)$$

where

$$\nu_t = C_R \Delta^2 (2\tilde{S}_{ij}\tilde{S}_{ij})^{1/2}, \quad k^{\text{SGS}} = C_I \Delta^2 (2\tilde{S}_{ij}\tilde{S}_{ij})$$

C_R and C_I are dimensionless constants determined empirically and take the values of 0.01 and 0.007, respectively. The strain-rate tensor $\tilde{S}_{ij} = (\partial \tilde{u}_i / \partial x_j + \partial \tilde{u}_j / \partial x_i) / 2$ and the symbol Δ denotes the filter width. Generally, the subgrid energy flux term is modeled as

$$H_i^{\text{SGS}} = -\rho \frac{-\nu_t}{\text{Pr}_t} \left(\frac{\partial \tilde{h}}{\partial x_j} + \tilde{u}_i \frac{\partial \tilde{u}_i}{\partial x_j} + \frac{1}{2} \frac{\partial k^{\text{SGS}}}{\partial x_j} \right) \quad (8)$$

where the turbulent Prandtl number is 0.7. The unclosed subgrid viscous-work term σ_{ij}^{SGS} is small compared to the other terms and is always neglected for simpleness. The detail of dynamic Smagorinsky model is given by Lilly [31].

Finally, the set of governing equations is closed using the equation of state. To correctly evaluate the thermodynamic properties at high-pressure conditions, a real fluid equation of state is required. The 32-term Benedict–Webb–Robin [32] equation of state has high accuracy for all conditions, but the equation is complicated and requires high computational expense, instead, the cubic equation of state is considered as a suitable choice. In the present study, the Soave–Redlich–Kwong (SRK) [33, 34] equation is adopted to calculate the thermodynamic and transport properties because it is accurate in both transcritical and supercritical conditions and easier to implement. The form of SRK equation can be written as,

$$p = \frac{\rho RT}{W - b\rho} - \frac{a\alpha}{W} \frac{\rho^2}{(W + b\rho)} \quad (9)$$

where R denotes the universal gas constant. The parameters a and b , which accounted for the effects of attractive and repulsive forces between molecules, take the following form,

$$a = 0.42747 \left(\frac{R^2 T_c}{p_c} \right) \text{ and } b = 0.08664 \left(\frac{RT_c}{p_c} \right) \quad (10)$$

where T_c and P_c are the critical temperature and pressure, respectively. In Eq. (9), α is defined as,

$$\alpha = \left[1 + S \left(1 - \sqrt{\frac{T}{T_c}} \right) \right]^2 \quad (11)$$

where

$$s = 0.48508 + 1.55171\omega - 0.15613\omega^2 \quad (12)$$

Based on the real fluid equation of state, the density effects under high-pressure conditions on thermodynamic properties, such as internal energy, constant-pressure specific heat, and entropy, are taken into account. The detailed expressions of these properties are available in Zong and Yang [16]. In this paper, the viscosity is determined by using the model of Zéberg-Mikkelsen et al. [35], while the thermal conductivity is evaluated by the model suggested by Vasserman and Nedostup [36].

3. Numerical method and implementation

3.1. Numerical method

The filtered compressible Navier–Stokes equations are solved using a finite-volume methodology. To achieve high accuracy for LES, the general low dissipation centered schemes are employed. Thus, second-order central difference schemes are used to approximate the convective and viscous terms, along with a second-order implicit scheme for temporal derivatives. However, the thermodynamic non-idealities, transport anomalies, and steep density gradient pose a big challenge for the numerical method [37]. The PISO algorithm is an efficient way to solve unsteady problem and has been widely used in computational fluid dynamics. The PISO algorithm is slightly modified by Park [18] to adapt to the large density ratio of supercritical fluid flows. In the present study, the modified form of PISO

algorithm is applied, also the artificial viscosity is used to avoid spurious oscillations, for more details of this algorithm the reader can refer to Park's works [18]. To improve the computation efficiency, a multiblock domain decomposition technique with message passing interfaces (MPI) is used for parallel computing.

The physical model simulated in this study is the experiment by Chehroudi et al. [5, 6] where the cryogenic nitrogen is injected into a warm nitrogen environment with the pressure and temperature exceeding its critical values ($P_c = 3.4$ MPa and $T_c = 126.3$ K). The chamber pressure and temperature are kept at constant values of 6.9 MPa and 300 K, respectively, and the cryogenic nitrogen at 120 K and 150 K is injected through a circular tube with a diameter $D_{inj} = 0.254$ mm into a chamber in supercritical state. The operating conditions are listed in Table 1, where the subscripts ∞ and inj denote the environment and injection conditions, respectively. These two cases are chosen because they are located to either side of the pseudo-boiling point (142 K), hence the two cases correspond to transcritical and supercritical injection, respectively.

The computational domain downstream of the nozzle is $40D_{inj}$ in length and with a diameter of $12D_{inj}$, which is sufficient to eliminate the influence of far-field boundary conditions on the near-injector flow. The three-dimensional domain is discretized by a grid system of $250 \times 100 \times 80$, which is within the range of inertial sub-range of turbulent kinetic energy spectrum. Constant temperature and velocity are sustained at the inlet, and a prescribed pressure for the outlet. The walls are considered as adiabatic walls and the injection is considered to be a fully developed turbulent flow.

Before proceeding further, it is important to validate the reliability and accuracy of numerical procedure with SRK equation of state. Figure 1 shows the density, constant-pressure specific heat, thermal conductivity, and viscosity in the temperature range 110–300 K at pressure of 6.9 MPa. Also, these thermodynamics and transport properties based on the ideal gas equation of state are given and compared with NIST measurement data [26]. As can be seen from the figure, the thermodynamics and transport properties are well reproduced by the SRK EOS and agree well with the NIST data, but the ideal gas EOS significantly underestimates the values. Although there are some discrepancies for the SRK EOS, especially for the constant-pressure specific heat around its pseudo-boiling point ($T^* = 141$ K), they follow the same trend well. The maximum constant-pressure specific heat can be obtained at the pseudo-boiling point corresponding to the prescribed pressure, which has important effects on the flow evolution. For the present study, the injection temperatures $T_{inj} < T^*$ (case 1) and $T_{inj} > T^*$ (case 2) correspond to the subcritical and supercritical injections, respectively.

3.2. Numerical scheme validation

For the purpose of testing the numerical scheme, a classical shock tube problem simulated by Arina [38] with a conventional low scheme (AUSMDV with MUSCL) under supercritical thermodynamic condition is used to validate the numerical method mentioned above. As an example, a computation based on the PR and SRK equation of state with carbon dioxide as working fluid is carried out. For comparison, the present computations are conducted with the same initial and boundary conditions. The critical pressure, temperature, and density of CO_2 are 7.37 MPa, 304.22 K, and 348.8 kg/m^3 , respectively. For the beginning, a long shock tube is split into two uniform regions with a diaphragm, where a shock and a contact discontinuity emerge by removing the diaphragm. The initial conditions are taken as

$$(\rho, u, p) = \begin{cases} (\rho_0, 0, 10 p_0), & 0 \leq x \leq 5 \\ (0.01 \rho_0, 0, 0.1 p_0), & 5 \leq x \leq 10 \end{cases} \quad (13)$$

Table 1. Physical parameters for simulation.

Case	T_{inj} (K)	u_{inj} (m/s)	T (K)	p (atm)	ρ_{inj}/ρ_{∞}	Re_{inj}
1	120	15	300	69	7.8	44,700
2	150	15	300	69	3.7	42,300

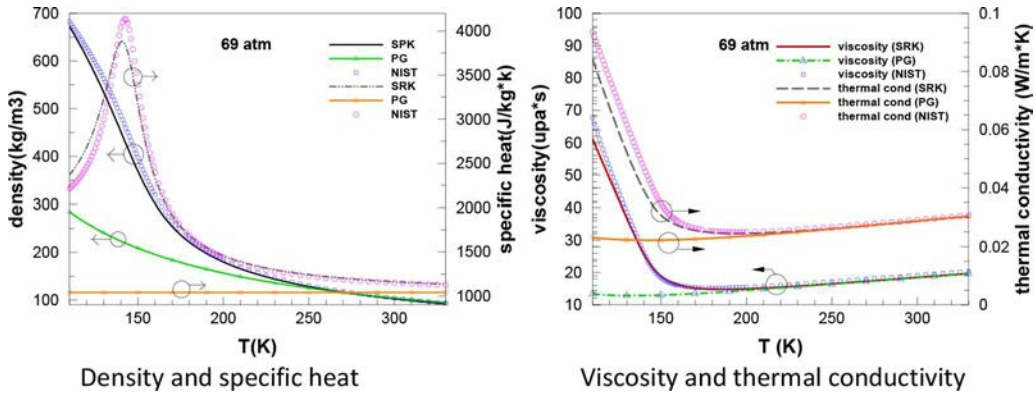


Figure 1. Comparison of the predicted density, constant-pressure specific heat, viscosity, and conductivity with NIST data for supercritical nitrogen.

where ρ_0 and p_0 take the value at the critical point. As suggested by Terashima [39], using the error function $\text{erf}(x)$ to smooth the initial interface is an effective way to avoid initial startup error. The error function is defined as,

$$q = q_L(1 - f_{sm}) + q_R f_{sm}, \quad f_{sm} = \frac{1 + \text{erf}[\Delta R/\varepsilon]}{2} \quad (14)$$

where q_R and q_L denote the left and right quantities, respectively. ΔR is the distance from the initial interface, and Δx is the grid spacing. ε is defined as $\varepsilon = C\Delta x$, where C is a free parameter. Different smoothness effects are obtained by adjusting the free parameter C . The computations are performed on a uniform grid, with 2,000 grid points. The free parameter $C = 3.0$.

Figures 2–4 show the normalized density, pressure, and velocity profiles calculated with different equations of state, respectively. For comparison, the results of Arina [38] with the Redlich–Kwong equation of state are also plotted. The present result evaluated by a second-order scheme is in good agreement with the reference solution. By a close-up view, it can be observed that the minor differences exist between the present results and Arina's due to the different cubic equations of state. Results obtained by solving the Riemann problem demonstrate that the numerical method is applicable for large density gradient and shock wave problem.

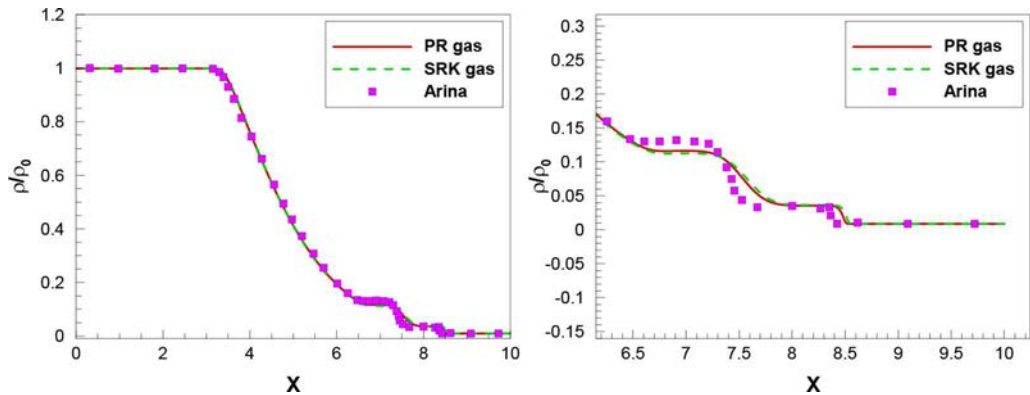


Figure 2. Normalized density distribution for Riemann problem; right: close-up view.

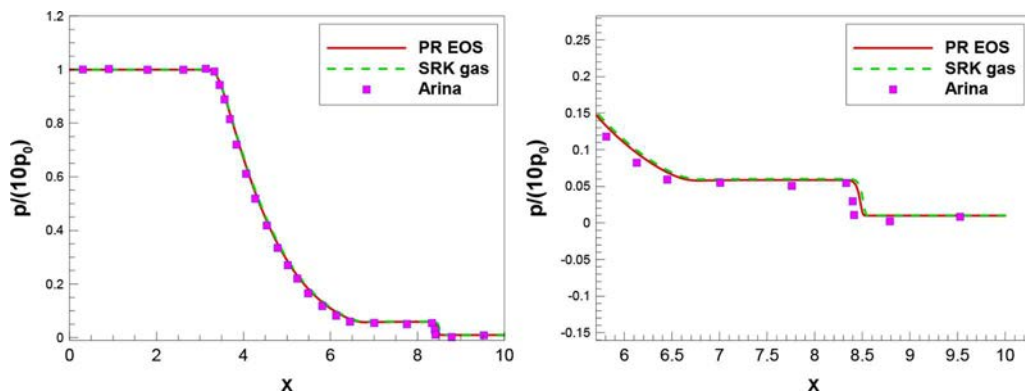


Figure 3. Normalized pressure distribution for Riemann problem; right: close-up view.

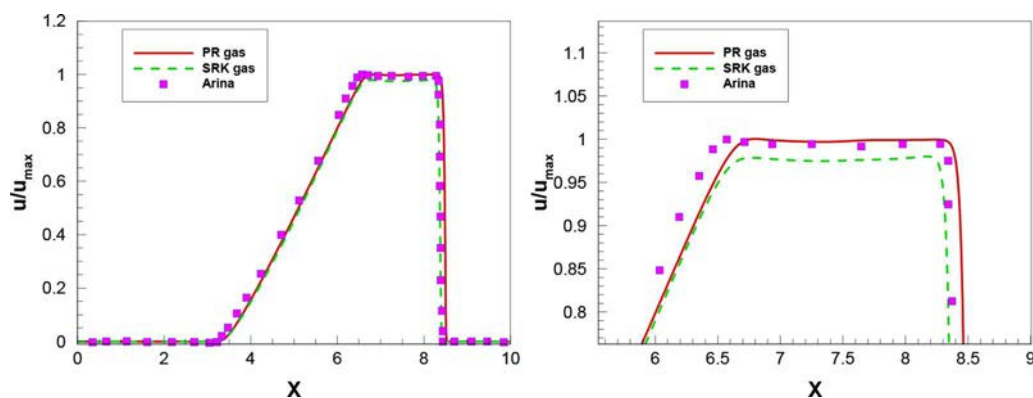


Figure 4. Normalized velocity distribution for Riemann problem; right: close-up view.

4. Results and discussion

4.1. Instantaneous flow field

Figure 5 presents snapshots of predicted vorticity magnitude, temperature, compressibility, and constant-pressure specific heat after the flow field reaches its stationary state for case 1 and case 2. It is well known that shear layer is very susceptible to the Kelvin–Helmholtz instability, stirring up the vortex rolling, paring, and breakup under low-pressure conditions. The same mechanism is also true for supercritical conditions. As shown in the vorticity plot in both cases, the vortex grows up at around five times the injector diameter for case 1 (four times for case 2) and pair with its adjacent vortex, resulting in large-scale vorticity structure. The generation and motion of large vortex facilitate the jet mixing with the surrounding gas and promote the entrainment of warmer environment gas into the jet.

As seen from the contour plot of temperature for the two cases, the temperature of supercritical injection (case 2) increases more rapidly indicating more intensive mixing feature downstream and accordingly showing a wider spreading domain. For the supercritical injection condition, the small-scale instable waves easily arise and roll into a string of vortices due to the lower density ratio between the jet and surrounding gas. Besides, the injection temperature in case 2 is above the pseudo-critical point (142 K), at which the maximum constant-pressure specific heat is attained. So the absorbed energy of the fluid is fully used to increase the jet temperature. On the contrary, through the injection process, the subcritical injection will across the pseudo-boiling point, consequently,

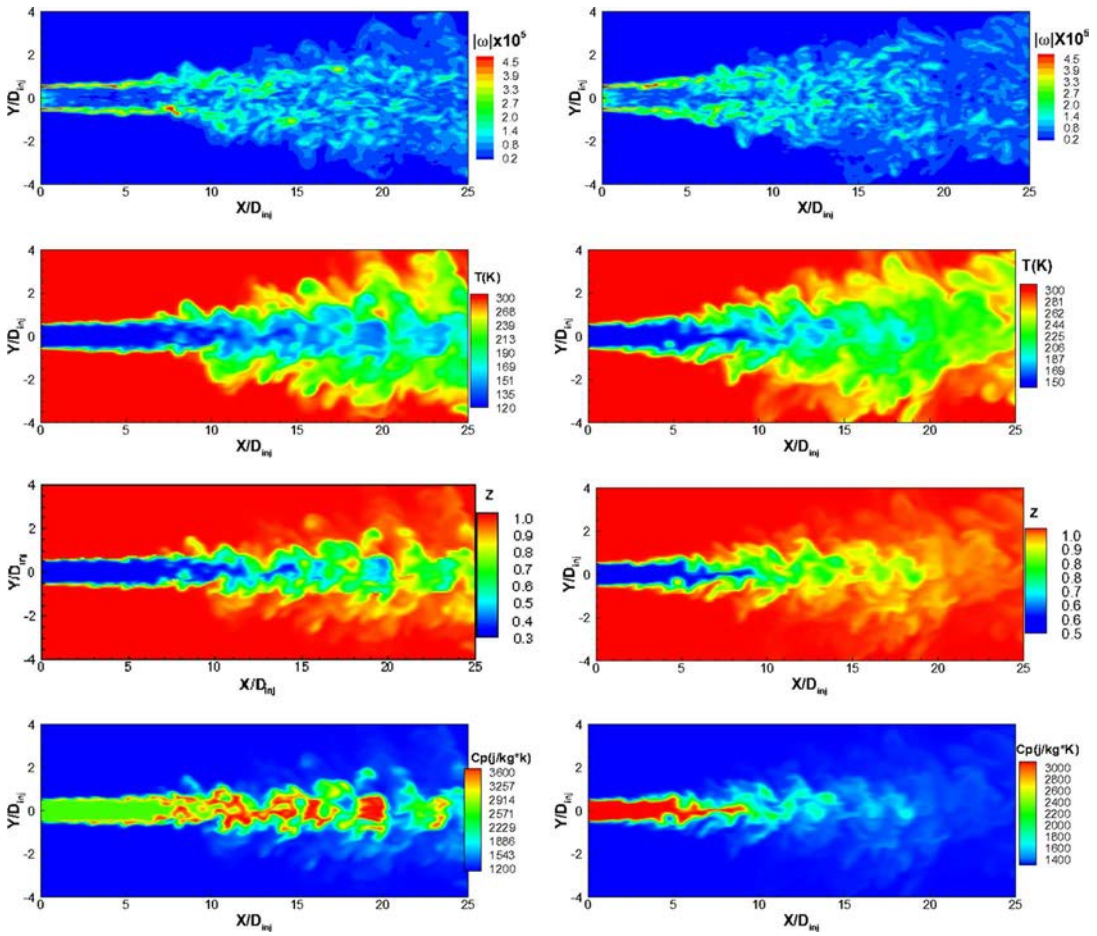


Figure 5. Snapshots of temperature, compressibility, constant-pressure specific heat, and vorticity magnitude for case 1 (left column) and case 2 (right column).

the energy is not only used to increase the temperature but also to expand the volume. Furthermore, the injection density ratio between injection and reservoir conditions is much higher for case 1 ($\rho_{inj}/\rho_{\infty} = 7.8$) than that for case 2 ($\rho_{inj}/\rho_{\infty} = 3.7$). Thus, a longer undisturbed liquid core is detected for the transcritical condition.

For the constant-pressure specific heat, as the jet is heated, the maximum value is located around the jet surface as well as at the end of the jet, indicating that at these locations the fluid is experiencing the pseudo-boiling. In the supercritical case, on the contrary, the maximum value of the constant-pressure specific heat is lower than in case 1 and concentrated in the core region of the jet downstream of the nozzle, followed by a continuous decline.

Compressibility is used to measure the compress level and plays an important role in describing supercritical fluid behaviors. The compressibility is defined as $Z = Pv/(RuT)$, where p , v , T , and Ru denote pressure, volume, temperature, and universal gas constant, respectively. For an ideal gas, the compressibility is equal to unity, while the value lower than unity indicates a departure from perfect gas. For both cases, as the jet mixes with the ambient gas, the compressibility increases from the jet core toward the outside due to the increase of temperature. For the different injection temperature of the two cases, it is noteworthy that the compressibility in the jet core region of case 2 is as large as two times of that of case 1, which is a significant difference between subcritical fluid and supercritical one. From the viewpoint of the pseudo-boiling, at which the most energy is absorbed to expand the

volume without increasing the temperature and, hence, the compressibility is significantly influenced by the pseudo-boiling phase change from liquid-like to gas-like. Thus, the strong departure from ideality behavior indicates that the real gas equation of state plays an important role and is essential in mathematical description of the present situation.

Figure 6 shows the iso-surfaces of $\rho_{1/2} = 0.5(\rho_\infty + \rho_{inj})$ and $\rho = 100 \text{ kg/m}^3$ for case 1 and case 2. For both cases, the outer side of the jet surface is twisted by the coherent structures and becomes irregular in spatial evolution as shown by the density iso-surfaces $\rho = 100 \text{ kg/m}^3$, which facilitate the mixing of the cryogenic fluid with the ambient nitrogen and promotes a rapid heat transfer. As the injected fluid moves downstream, a series of dense fluid pockets sheds from the core region and dissolves into the environment. Comparing the two cases, a much longer dense core is detected for case 1, this is because of the lower injection temperature corresponding to a larger density ratio, which is an important factor for the generation of large density gradient.

Figure 7 presents the snapshots of density gradient in the middle plane for case 1 and case 2. Similar to the iso-surface, the density gradient has a perceptual intuition to the shadow-graph-like images that can be observed in the experiment by Chehroudi under the same conditions. For both cases, the jet surfaces are surrounded by large density gradients, and this value is much larger for the transcritical case (case 1), indicating that larger density stratification leads to stronger density gradient. High density gradient has the effects of stabilizing the flow field by suppressing radial velocity fluctuations and inhibiting the development of instable waves. Thus, the delayed transition to fully developed flow results in a longer potential core, around $8D_{inj}$ for case 1, while about $6D_{inj}$ for case 2. For the transcritical case, the dashed line corresponds to the pseudo-boiling temperature and is mainly distributed in the large density gradient region, indicating that besides density ratio, the pseudo-boiling temperature has some effects on forming high density gradient. To identify the formation of the large density stratification in case 1, conditional-averaged constant-pressure specific heat over regions where density gradient magnitudes exceed pre-specified cutoff are given in Table 2. In the table, the conditional-averaged specific heat increases with increasing the cutoff density gradient, implying that large specific heat have some effect of producing large density stratification.

Figure 8 presents the instantaneous iso-surfaces of Q value for two cases. The Q -criterion is applied to capture the coherent structure and the process of its evolution in the flow field. For both cases, as Q is smaller ($1 \times 10^8 \text{ s}^{-2}$), a large number of different scales of coherent structures are identified and mainly distributed around the jet surface and far away from the jet core. When the Q value increases

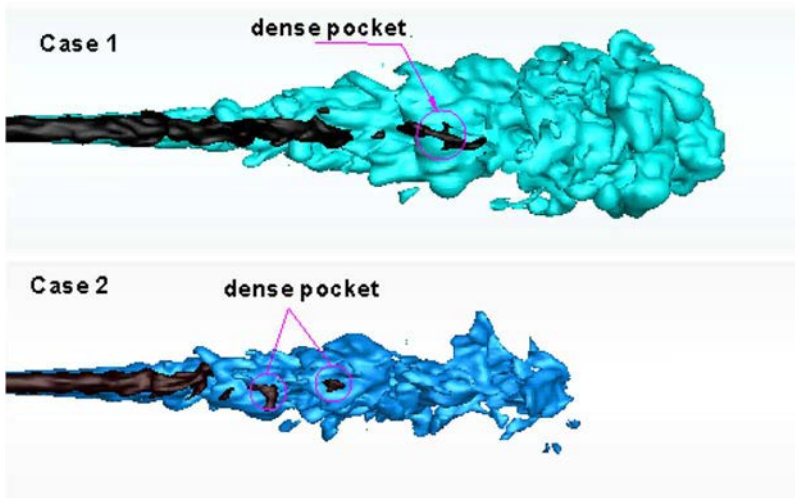


Figure 6. Instantaneous density iso-surface of $\rho_{1/2} = 0.5(\rho_\infty + \rho_{inj})$ (the dark ones) and $\rho = 100 \text{ kg/m}^3$ (the blue ones) for case 1 (top) and case 2 (bottom).

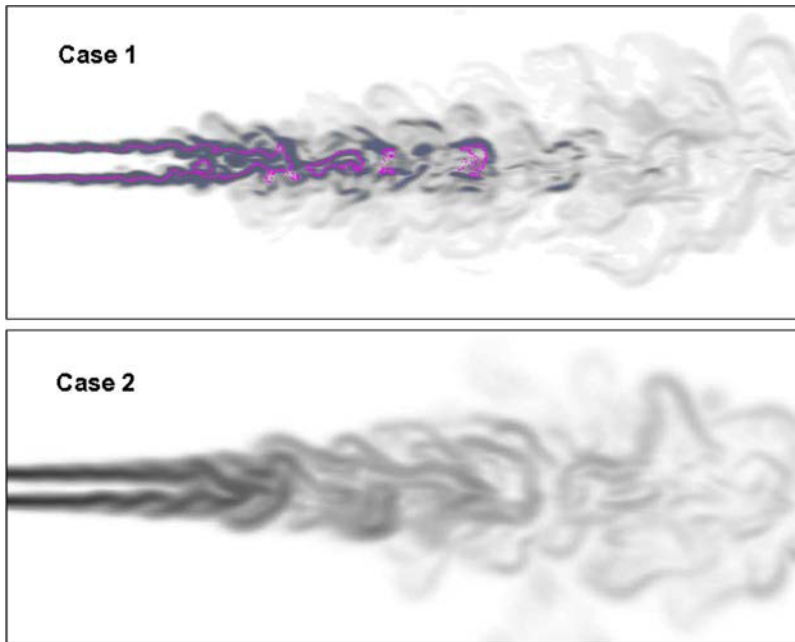


Figure 7. Numerically reconstructed shadowgraphs of case 1 (the pink line corresponds to the pseudo-boiling temperature) and case 2 over a distance of 20 injector diameters.

to 5×10^8 and $9 \times 10^8 \text{ s}^{-2}$, the small-scale structures are more and more filtered out and the large-scale coherent structures exist in the central regions near the jet inlet, where the vortex pairing is prevailing and dominate the mixing between the jet and ambient gas at this stage. As the large vortex develops downstream, the stretching effect plays a dominant role and large-scale structures are teared up into small-scale structures and a large amount of small-scale structures emerge on the domain far from the jet inlet. Comparing the transcritical and supercritical cases, the coherent structures in the latter case tend to be generated more intensively because the growth rate of the vortex disturbances increase as the injection temperature increases.

4.2. Mean flow properties

To quantitatively characterize the jet mixing of supercritical fluid, time-dependent instantaneous quantities are collected to calculate the time average of flow properties after the flow reaches its stationary state. Figure 9 presents the normalized density and velocity along the centerline for the two cases. The density profile remains unchanged in the potential core, whose length is about $8D_{inj}$ and $6D_{inj}$ for case 1 and case 2, respectively, indicating that increasing the injection temperature has an effect of decreasing the density stratification and then downsizing the potential core. For case 1, owing to the volume dilatation caused by the phase change, the density profile exhibits a severe drop at the end of the potential core, where the temperature transits across the pseudo-boiling point. On the other hand, the injection temperature in case 2 is above the pseudo-boiling point, so though it also shows a sharp drop, it is induced by a different reason, that is, a rapid mixing between the dense core and surrounding gas. The same phenomenon is true for the velocity profiles. For comparison, the

Table 2. Conditional averaged constant-pressure specific heat in $|\nabla p|$.

Cutoff	$0.1 \nabla p $	$0.3 \nabla p $	$0.9 \nabla p $
C_p (J/g*K)	3.052	3.480	3.782

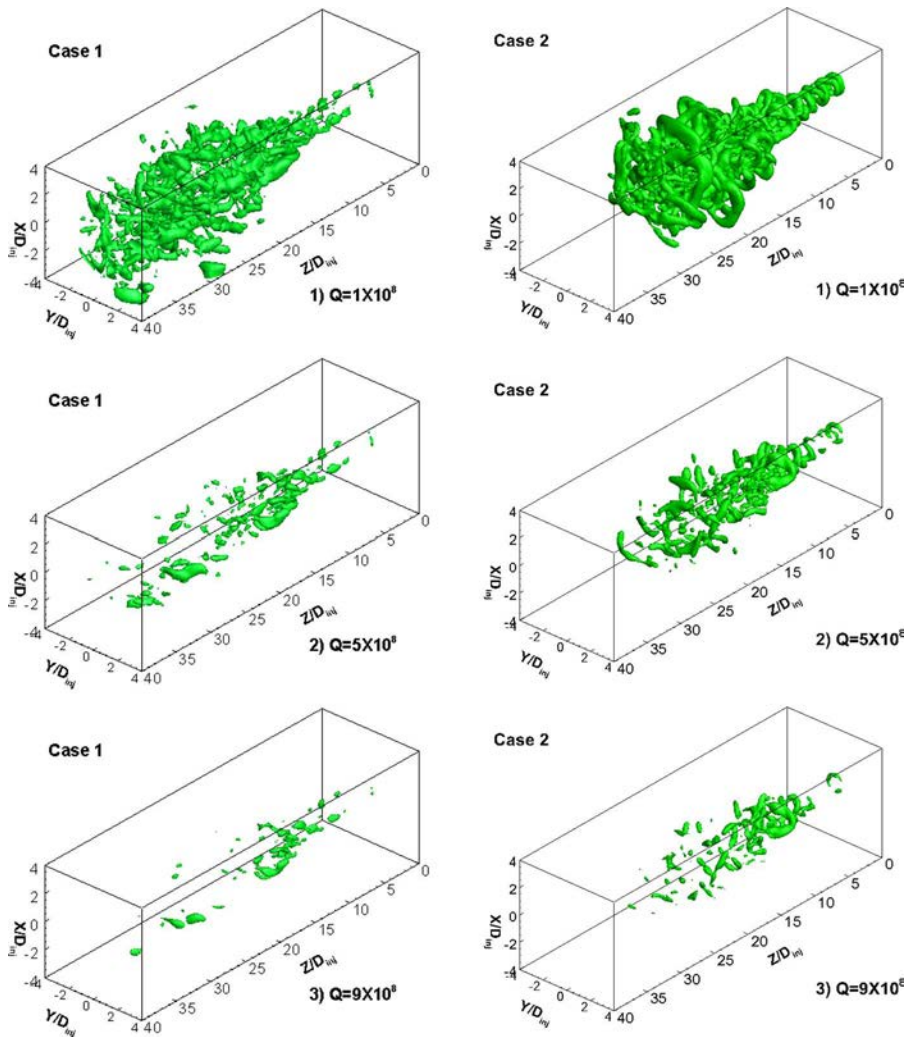


Figure 8. Comparison of the instantaneous iso-surface of Q value for two cases.

simulation results of Zong et al. [16] are also presented for case 1. The simulation results obtained here agree well with Zong's study. In addition, the normalized turbulent kinetic energy and constant-pressure specific heat along the centerline are also presented in Figure 6. For the turbulent kinetic energy, both cases exhibit similar trends with a very small initial region followed by a steep increase and a gradual decrease toward a plateau region. The initial region is longer for case 1, which corresponds to the longer potential core. In both cases the peak values of the kinetic energy appear at the locations downstream of the ends of potential cores. Besides, the supercritical case shows a higher peak and faster drop than the transcritical case. In constant-pressure specific heat profiles, the evolution tendency of the two cases exhibit a significant difference: in case 1 there is a notable peak that is absent in case 2. This is caused by the temperature transition across the pseudo-boiling point, where heat transfer from the environment does not increase the jet temperature but merely expands fluid volume. However, in case 2 the constant-pressure specific heat profile decreases smoothly without a peak zone since the initial injection temperature is already above the pseudo-boiling temperature.

Figure 10 shows the radial distributions of viscosity and thermal conductivity. One obvious phenomenon is that a minimum value exists in case 1, which is caused by the temperature transition across the pseudo-boiling temperature, while for case 2, the temperature is above the pseudo-boiling

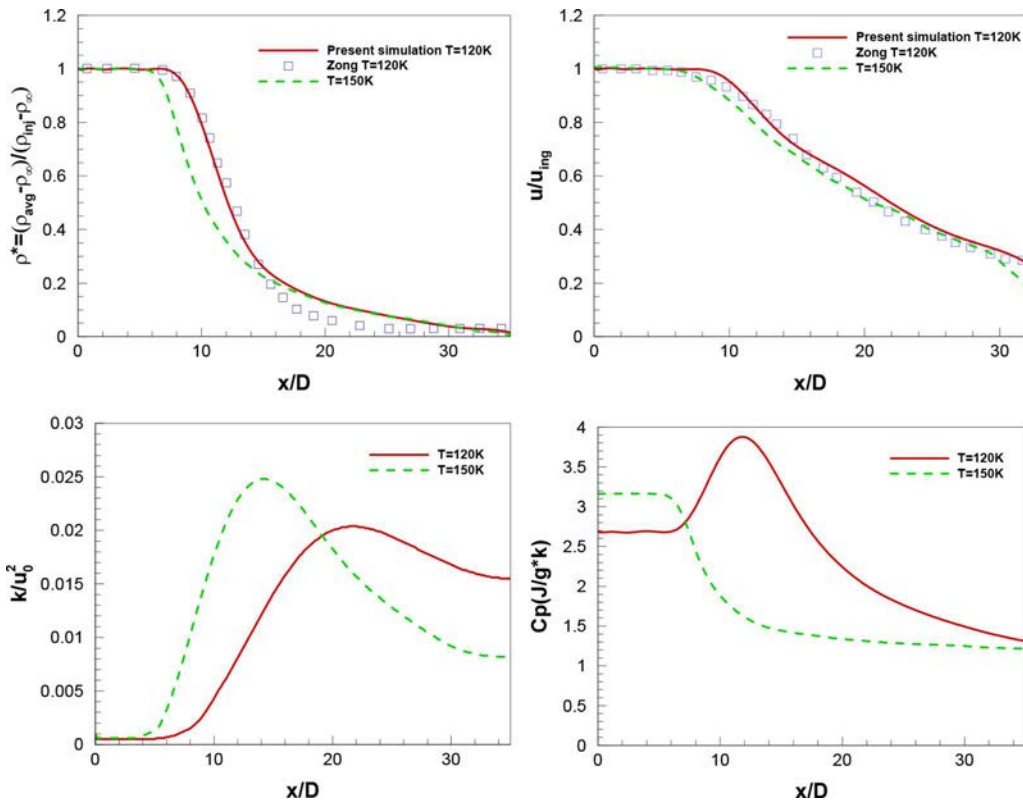


Figure 9. Effect of temperature on the normalized density, velocity, turbulent kinetic energy, and constant specific heat along the centerline.

point, so the viscosity and thermal conductivity initiate with a constant value followed by gradual increase to a horizontal level, which is in accordance with the temperature evolution tendency across the lateral section of the jet. This suggests that the pseudo-boiling point has the effects of influencing the transport properties, and then the supercritical jet evolution.

Figure 11 shows the radial profiles of the root mean square of density and temperature. These thermodynamic values are normalized by its injection conditions. At the location of $x/D_{inj} = 5$, which is in the potential core region, a spike exists in the root mean square density around the boundary of the jet surface for both cases, however, the peak value in case 1 is much higher than that in case 2,

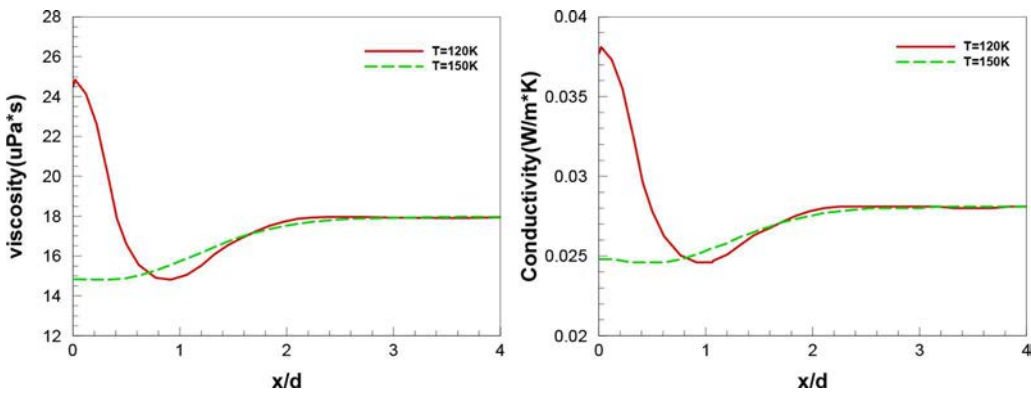


Figure 10. Radial distributions of viscosity and thermal conductivity at $x/d = 12$.

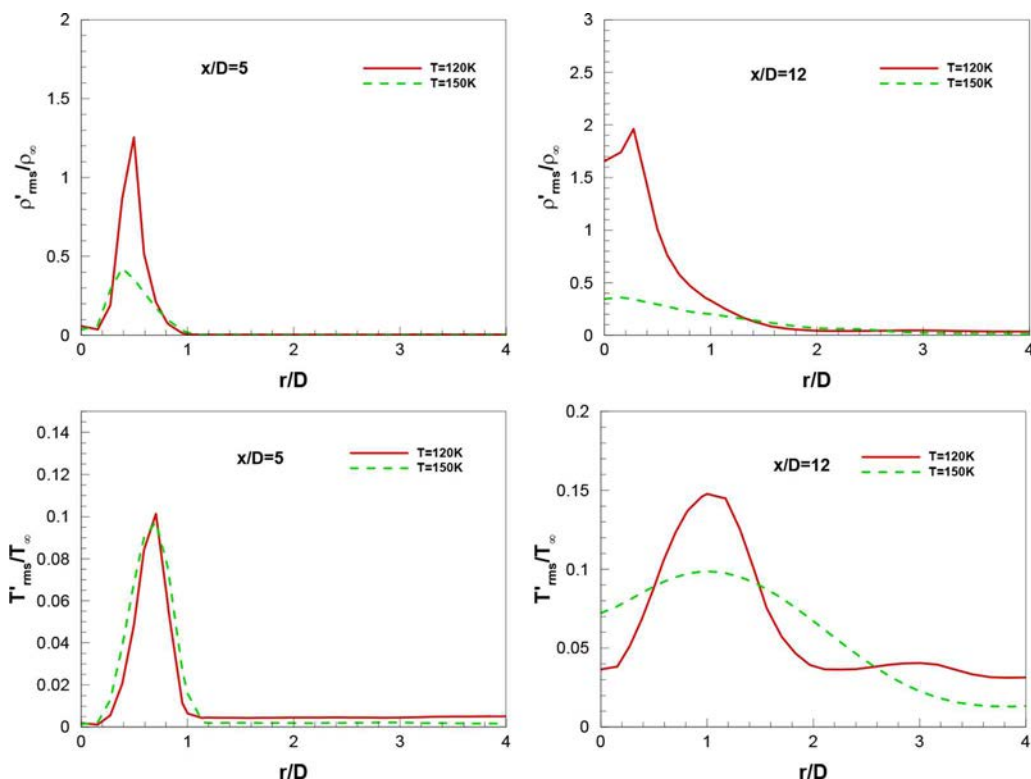


Figure 11. The root mean square values of the fluctuation of density and temperature along the radial profiles at different axis positions.

indicating that the higher density ratio has an effect of increase in the density fluctuation. By close inspection, the peak value of the transcritical case slightly moves to the right gas side indicating that as the jet boundary is heated, energy is absorbed to expand the jet volume because the injection temperature is below the pseudo-boiling point. In the transition region of $x/D_{inj} = 12$, where the temperature transits across the pseudo-boiling point (see Figure 5), very high density fluctuation exists in the jet center along with a spike on the core surface and followed by a sharp decrease toward zero. At the two locations, the density fluctuation maxima reaches about 1.75 and 2.0, implying extremely strong turbulent fluctuations. The situation is different with the supercritical injection condition, where the maximum value is in the centerline followed by a gradual decrease to zero. By comparing the two cases, the transcritical case has a much more intensive density fluctuation than the supercritical one. Compared to the density, the temperature fluctuation is more moderate. At $x/D = 5$, the temperature fluctuation distribution nearly merges to one line, this implies the injection temperature has little effect on temperature fluctuation in the potential core regions. However, at the transition region of $x/D = 12$, both cases start with similar trends with a certain value followed by a gradual increase and then a decrease toward a plateau, but the transcritical injection reaches a higher peak and steeper increase and decrease rates.

Traditionally, the spreading rate of a jet is used to measure the mixing efficiency. Generally, the density and velocity fields are applied to evaluate the spreading rate. In the present study, the calculation of spreading rate is based on the density field. Two criteria are available by using the density field. The first criterion is a length so-called half-width, half-maximum (HWHM) [4], L_p , which is defined as the median value between dense and light regions based on the cross-stream profiles of average density. The spreading rate $EH \rho$ is defined as the slope of the linear regression of L_p along the jet centerline, and the linear regression region begins with a linearly increase of L_p . The HWHM

spreading angle θ^H can be defined as

$$\theta^H = \arctan(E_\rho^H) \quad (15)$$

- The second criterion for the density spreading rate can be obtained by a direct visualization of the flow. More detailed descriptions of this criterion is given by Schmitt [40]. The HWHM methodology can be extended to evaluate the half-width of the velocity profile at half the maximum L_u and the velocity spreading rate $EH\ u$ is obtained by the same way.

Figure 12 shows the evolution of jet HWHM L_ρ and HWHM density spreading rate $EH\ \rho$ along the jet centerline. For HWHM L_ρ , initially the jet keeps a constant value, which is corresponding to the potential core, and then followed by a linear increase for two cases. The simulation results conducted by Zong are given as well, and the HWHM L_ρ obtained in the present study show good agreement with Zong's study. Compared to the transcritical case, the supercritical case contains a shorter initial constant value and broader HWHM L_ρ . This means that the high-temperature injection can lead to a faster transition and facilitate the jet mixing with the ambient gas. The spreading rate $EH\ \rho$, which is defined as the slope of the linear regression of L_ρ , is used to evaluate the spatial growth rate of a jet flow. The spreading rate $EH\ \rho$ of the two cases are given in Figure 8 (left). For comparison, the existing experiment, simulation data (both low- and high-pressure), and the empirical correlation proposed by Chen and Rodi are presented as a function of the density ratio. The two cases in the present study are quite consistent with the empirical correlation proposed by Chen and Rodi at around 0.11, and the same is true for all the other experiment and calculation cases except for Mayer's case [41], where the distributions are extremely scattered and there is no explanation for this discrepancy to date. By careful comparison, the discrepancy among the small density ratio case (Richard and Pitts, $\rho_{inj}/\rho = 1-2.3$) [42], the dense case (Oschwald and Micci, $\rho_{inj}/\rho = 10-13$) [8], and the supersonic mixing layer or jet ($\rho_{inj}/\rho = 1-6.8$) [43] is not more than 8%. From the analysis above, the spreading rates of both the transcritical and supercritical injections are similar to those in low-pressure condition case, thus, the spreading rate is not sensitive to the temperature. That is to say the density ratio has a very limited impact on the spreading rate.

Figure 13 shows the radial distributions of normalized mean density at different axial positions for two cases. The radial coordinate is normalized by HWHM ($r_{1/2}$) at different axial positions of concern, and the mean density along the radial locations can be normalized as:

$$\rho^* = \frac{\bar{\rho} - \bar{\rho}_\infty}{\bar{\rho}_c - \bar{\rho}_\infty} \quad (16)$$

where $\bar{\rho}$, $\bar{\rho}_c$, $\bar{\rho}_\infty$ denote the radial mean density, center mean density, and ambient mean density, respectively. By careful inspection, the jet develops to three distinct flow regions, including the

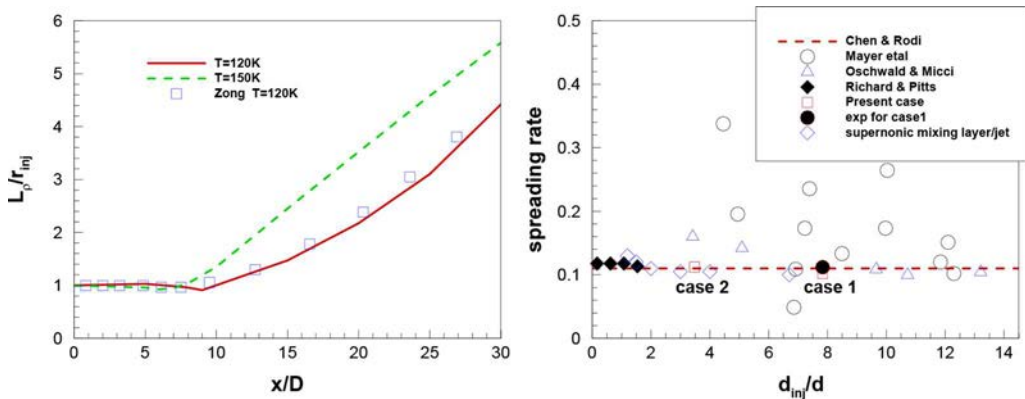


Figure 12. The evolution of jet HWHM L_ρ and HWHM density spreading rate $EH\ \rho$ along the jet centerline.

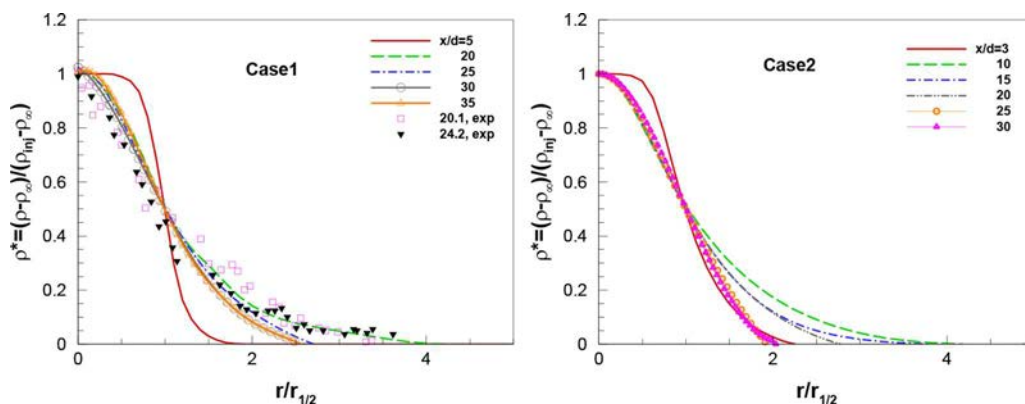


Figure 13. Radial distributions of normalized density at different axial locations.

potential core, transition, and self-similarity regions, which is similar to that of incompressible turbulent jets. A flat-hat appears at the location of $x/d = 5$, indicating that the jet fluid keeps its initial feature in the potential core region. As mentioned above, the potential core region can last as long as $8D_{inj}$ for case 1 and about $6D_{inj}$ for case 2. For the self-similarity regions, the two cases show different features, namely the density profiles merge into one line further downstream at $30D_{inj}$ for case 1, while at $25D_{inj}$ for case 2, suggesting that the high-temperature injection has the effect of speeding up the flow to develop into self-similarity region. Using the Raman scattering technique, Chehrودي et al. conducted an experiment on the conditions of case 1, and the experimental data are also plotted in Figure 13 for comparison. The present simulation ($x/d = 20$ and $x/d = 25$) follows the trend well and achieved a good agreement with the experiment ($x/d = 20.1$ and $x/d = 24.2$) with a maximum deviation less than 8.6%.

5. Conclusions

In the present study, a comparative study on the transcritical and supercritical injections of nitrogen is conducted using LES. Using the real gas equation of state, a general centered scheme with high accuracy and low dissipation was employed. The PISO algorithm was modified to handle real fluid state and the large density ratios for supercritical fluid injection. The inviscid Riemann problem was used to test the modified algorithm and demonstrated that it had the capacity to handle large density gradient and shock wave problems.

The different mixing features of transcritical and supercritical injection are studied in detail. As we know that when the fluid transits across the pseudo-boiling point, energy is consumed to expand the volume rather than to increase the temperature. So the pseudo-boiling phenomenon may have certain influence on the evolution of injection. For the transcritical injection, affected by the pseudo-boiling point, the constant-pressure specific heat reaches a local maximum, while the thermal conductivity and viscosity become minimums. While the phenomenon is absent for the supercritical injection conditions. Vorticity and Q-criterion analyses suggest that the jet surface more unstable with vorticity tends to grow up for the supercritical injection, and large number of coherent structures of different scales are easily formed. This characteristic indicates that higher-injection temperature above the pseudo-boiling point has the effects of enhancing the jet, whose volume has already considerably expanded, mixing with ambient fluid. The condition-averaged constant-pressure specific heat of transcritical injection shows that large specific heat concentrates on the high-density gradient regions, indicating that the pseudo-boiling point have certain influence on forming large-density gradient. Anyway, the transcritical injection shows higher-density gradient due to the initial larger-density stratification and the transition of the injected fluid across the pseudo-boiling point.

In terms of mean flow properties, in the transcritical injection, the mixing behavior is influenced by rapid variations of properties and large density gradient due to the large density ratio and the pseudo boiling point effects, showing longer potential core and slower transition. In addition, the root mean square of density fluctuation is sensitive to density ratio and thermodynamic properties, while the fluctuation temperature is moderately affected. Self-similar analysis suggests that the supercritical jet tends to transit into the self-similarity region. The spreading rates for both the transcritical and supercritical injections are analogous to that of low- and high-pressure variable density jets. This behavior indicates that the density ratio and properties across the transition region have little effect on the spreading rate. These observations can help to gain deeper understanding behavior of supercritical and transcritical injections, which is of importance in enhancing mixing efficiency between fuels and adjacent oxidizers for power generation machine.

Funding

This work is supported by National Natural Science Foundation of China (grant number 51376029).

References

- [1] S. Candel, M. Juniper, G. Singla, P. Scoufflaire, and C. Rolon, Structure and Dynamics of Cryogenic Flames at Supercritical Pressure, *Combust. Sci. Technol.*, vol. 178, no. 1–3, pp. 161–192, 2006.
- [2] D. T. Banuti, Crossing the Widom-Line – Supercritical Pseudo-Boiling, *J. Supercrit. Fluids*, vol. 98, pp. 12–16, 2015.
- [3] G. G. Simeoni, T. Bryk, F. A. Gorelli, M. Krisch, G. Ruocco, M. Santoro, and T. Scopigno, The Widom Line as the Crossover Between Liquid-Like and Gas-Like Behaviour in Supercritical Fluids, *Nat. Phys.*, vol. 6, no. 7, pp. 503–507, 2010.
- [4] R. Branam and W. Mayer, Characterization of Cryogenic Injection at Supercritical Pressure, *J. Propul. Power*, vol. 19, no. 3, pp. 342–355, 2003.
- [5] B. Chehroudi, R. Cohn, and D. Talley, Cryogenic Shear Layers: Experiments and Phenomenological Modeling of the Initial Growth Rate Under Subcritical and Supercritical Conditions, *Int. J. Heat Fluid Flow*, vol. 23, no. 5, pp. 554–563, 2002.
- [6] B. Chehroudi, D. Talley, and E. Coy, Visual Characteristics and Initial Growth Rates of Round Cryogenic Jets at Subcritical and Supercritical Pressures, *Phys. Fluids (1994-present)*, vol. 14, no. 2, pp. 850–861, 2002.
- [7] W. Mayer, J. Telaar, R. Branam, G. Schneider, and J. Hussong, Raman Measurements of Cryogenic Injection at Supercritical Pressure, *Heat Mass Transfer*, vol. 39, no. 8–9, pp. 709–719, 2003.
- [8] M. Oschwald and M. Micci, Spreading Angle and Centerline Variation of Density of Supercritical Nitrogen Jets, *Atomization Sprays*, vol. 12, no. 2002, pp. 91–106, 2002.
- [9] M. Oschwald and A. Schik, Supercritical Nitrogen Free Jet Investigated by Spontaneous Raman Scattering, *Exp. Fluids*, vol. 27, no. 6, pp. 497–506, 1999.
- [10] M. Oschwald, J. J. Smith, R. Branam, J. Hussong, A. Schik, B. Chehroudi, and D. TAAley, Injection of Fluids into Supercritical Environments, *Combust. Sci. Technol.*, vol. 178, no. 1, pp. 49–100, 2004.
- [11] R. S. Miller and J. Bellan, Direct Numerical Simulation of a Confined Three-Dimensional Gas Mixing Layer with One Evaporating Hydrocarbon-Droplet-Laden Stream, *J. Fluid Mech.*, vol. 384, no. 7, pp. 293–338, 1999.
- [12] R. S. Miller, K. G. Harstad, and J. Bellan, Direct Numerical Simulations of Supercritical Fluid Mixing Layers Applied to Heptane & #8211; Nitrogen, *J. Fluid Mech.*, vol. 436, no. 4, pp. 1–39, 2001.
- [13] N. A. Okong’O and J. Bellan, Direct Numerical Simulation of a Transitional Supercritical Binary Mixing Layer: Heptane and Nitrogen, *J. Fluid Mech.*, vol. 464, no. 10, pp. 1–34, 2002.
- [14] J. Oefelin, Analysis of Transcritical Spray Phenomena in Turbulent Mixing Layers, *AIAA J.*, 96-0085 34, 1996.
- [15] N. Zong, H. Meng, S. Y. Hsieh, and V. Yang, A Numerical Study of Cryogenic Fluid Injection and Mixing Under Supercritical Conditions, *Phys. Fluids*, vol. 16, no. 12, pp. 4248–4261, 2004.
- [16] N. Zong and V. Yang, Cryogenic Fluid Jets and Mixing Layers in Transcritical and Supercritical Environments, *Combust. Sci. Technol.*, vol. 178, no. 1, pp. 193–227, 2006.
- [17] T. Kim, Y. Kim, and S. K. Kim, Numerical Study of Cryogenic Liquid Nitrogen Jets at Supercritical Pressures, *J. Supercrit. Fluids*, vol. 56, no. 2, pp. 152–163, 2011.
- [18] T. S. Park, LES and RANS Simulations of Cryogenic Liquid Nitrogen Jets, *J. Supercrit. Fluids*, vol. 72, no. 12, pp. 232–247, 2012.
- [19] S. Laurent and G. Ribert, Equation of State Effects for Turbulent Flows Under Supercritical Conditions and their Impact on Modeling Strategies, 2nd Colloque INCA, Rouen, France, 2008.

- [20] C. A. Niedermeier, N. A. Adams, M. M. Jarczyk, M. Pfitzner, and S. Hickel, Large Eddy Simulation of Oxygen/Hydrogen Mixing Layers under Supercritical Conditions.
- [21] L. Selle and D. G. Ribert, Modeling Requirements for Large-Eddy Simulation of Turbulent Flows Under Supercritical Thermodynamic Conditions, Summer Program, Center for Turbulence Research, *Proceedings of the Summer Program*, pp. 195–207, 2008.
- [22] L. Selle and T. Schmitt, Large-Eddy Simulation of Single-Species Flows Under Supercritical Thermodynamic Conditions, *Combust. Sci. Technol.*, vol. 182, no. 4, pp. 392–404, 2010.
- [23] A. Keshmiri, K. Osman, S. Benhamadouche, and N. Shokri, Assessment of Advanced RANS Models Against Large Eddy Simulation and Experimental Data in the Investigation of Ribbed Passages with Passive Heat Transfer, *Numer. Heat Transfer Part B Fundam. Int. J. Comput. Method.*, vol. 69, no. 2, pp. 96–110, 2016.
- [24] A. C. Y. Yuen, G. H. Yeoh, V. Timchenko, and T. Barber, LES and Multi-Step Chemical Reaction in Compartment Fires, *Numer. Heat Transfer Appl.*, vol. 68, no. 7, pp. 711–736, 2015.
- [25] Y. M. Yin and X. Y. Lu, Effects of Injection Temperature on the Jet Evolution Under Supercritical Conditions, *Chin. Sci. Bull.*, vol. 54, no. 22, pp. 4197–4204, 2009.
- [26] K. Li and L. X. Zhou, Studies of the Effect of Spray Inlet Conditions on the Flow and Flame Structures of Ethanol-Spray Combustion by Large-Eddy Simulation, *Numer. Heat Transfer Appl.*, vol. 62, no. 1, pp. 44–59, 2012.
- [27] X. Sun, C. K. Chan, B. Mei, and Z. Zhu, LES of Convective Heat Transfer and Incompressible Fluid Flow Past a Square Cylinder, *Numer. Heat Transfer Part A: Appl.*, vol. 69, no. 10, pp. 1106–1124, 2016.
- [28] L. Paniagua, O. Lehmkuhl, C. Oliet, and C. D. Pérez-Segarra, Large Eddy Simulations (LES) on the Flow and Heat Transfer in a Wall-Bounded Pin Matrix, *Numer. Heat Transfer Part B – Fundam.*, vol. 65, no. 2, pp. 103–128, 2014.
- [29] W.-S. Fu, C.-G. Li, M. Tsubokura, Y. Huang, and J. A. Domaradzki, An Investigation of Compressible Turbulent Forced Convection by an Implicit Turbulence Model for Large Eddy Simulation, *Numer. Heat Transfer Part A Appl. Int. J. Comput. Method.*, vol. 64, no. 11, pp. 858–878, 2013.
- [30] J. Smagorinsky, General Circulation Experiments with the Primitive Equations, *Mon. Weather Rev.*, vol. 91, no. 3, pp. 99–164, 1963.
- [31] D. K. Lilly, A Proposed Modification of the Germano Subgrid-Scale Closure Method, *Phys. Fluids A: Fluid Dyn.*, vol. 4, no. 3, pp. 633, 1992.
- [32] R. T. Jacobsen and R. B. Stewart, Thermodynamic Properties of Nitrogen Including Liquid and Vapor Phases from 63 K to 2000 K with Pressures to 10,000 Bar, *J. Phys. Chem. Ref. Data*, vol. 2, no. 4, 1973.
- [33] M. S. Graboski and T. E. Daubert, A Modified Soave Equation of State for Phase Equilibrium Calculations. 1. Hydrocarbon Systems, *Ind. Eng. Chem. Process Des. Dev.*, vol. 19, no. 3, pp. 429–435, 1980.
- [34] G. Soave, Equilibrium Constants from a Modified Redlich-Kwong Equation of State, *Chem. Eng. Sci.*, vol. 27, no. 6, pp. 1197–1203, 1972.
- [35] C. K. Zéberg-Mikkelsen, S. E. Quiñones-Cisneros, and E. H. Stenby, Viscosity Modeling of Light Gases at Supercritical Conditions Using the Friction Theory, *Ind. Eng. Chem. Res.*, vol. 40, no. 17, pp. 3848–3854, 2001.
- [36] A. A. Vasserman and V. I. Nedostup, An Equation for Calculation of the Thermal Conductivity of Gases and Liquids, *J. Eng. Phys.*, vol. 20, no. 1, pp. 89–92, 1971.
- [37] S. M. Yahya, S. F. Anwer, and S. Sanghi, LES of Stably Stratified Flow with Varying Thermophysical Properties, *Numer. Heat Transfer Appl.*, vol. 67, no. 12, pp. 1408–1427, 2015.
- [38] R. Arina, Numerical Simulation of Near-Critical Fluids, *Appl. Numer. Math.*, vol. 51, no. 4, pp. 409–426, 2004.
- [39] S. Kawai and H. Terashima, A High-Resolution Scheme for Compressible Multicomponent Flow with Shock Waves, *Internat. J. Numer. Methods Fluids*, vol. 66, no. 10, pp. 1207–1225, 2011.
- [40] T. Schmitt, L. Selle, A. Ruiz, and B. Cuenot, Large-Eddy Simulation of Supercritical-Pressure Round Jets, *AIAA J.*, vol. 48, no. 9, pp. 2133–2144, 2012.
- [41] W. Mayer, J. Telaar, R. Branam, G. Schneider, and J. Hussong, Raman Measurements of Cryogenic Injection at Supercritical Pressure, *Heat Mass Transfer*, vol. 39, no. 8–9, pp. 709–719, 2003.
- [42] C. D. Richards and W. M. Pitts, Global Density Effects on the Self-Preservation Behaviour of Turbulent Free Jets, *J. Fluid Mech.*, vol. 254, pp. 417–435, 1993.
- [43] G. L. Brown and A. Roshko, On Density Effects and Large Structure in Turbulent Mixing Layers, *J. Fluid Mech.*, vol. 64, pp. 775–816, 1974.

Copyright of Numerical Heat Transfer: Part A -- Applications is the property of Taylor & Francis Ltd and its content may not be copied or emailed to multiple sites or posted to a listserv without the copyright holder's express written permission. However, users may print, download, or email articles for individual use.